RSC Advances

PAPER

View Article Online
View Journal | View Issue

Cite this: *RSC Adv.*, 2025, **15**, 38624

Adsorption performance of zero-valent iron-loaded biochar for tetracycline antibiotics

Xingzhi Yang,†[a] Xichang Wu,†[b] Xinyun Liu,*[a] Yu Wang[b] and Anping Wang *[b]

Tetracycline hydrochloride (TCH) and oxytetracycline hydrochloride (OTC) are widely used tetracycline antibiotics in global livestock production and the medical field. However, due to their strong chemical stability and resistance to degradation, these antibiotics can cause severe environmental pollution. Adsorption technology is an effective method for removing these drugs from wastewater. In this study, hexahydrate ferric chloride ($FeCl_3 \cdot 6H_2O$), 2-methylimidazole ($C_4H_6N_2$), and potassium hydroxide (KOH) were used to modify biochar (BC) derived from *Camellia* seed shells, enhancing its adsorption performance for the TCH and OTC. The adsorption process primarily involves chemical adsorption and multilayer adsorption mechanisms. Solution pH significantly affects adsorption efficiency, with an optimum pH of 3. The maximum adsorption capacity for the TCH is 62.07 mg g^{-1}, while for the OTC it is 41.28 mg g^{-1}. An elevation in the operating temperature leads to a reduction in the adsorption capacity of TCH, while the adsorption capacity of OTC exhibits an initial decline followed by a subsequent increase. The adsorption mechanisms include $\pi-\pi$ interactions, electrostatic forces, and hydrogen bonding between the biochar and the antibiotics.

Received 19th June 2025
Accepted 9th October 2025

DOI: 10.1039/d5ra04362j

rsc.li/rsc-advances

1. Introduction

Following the discovery of penicillin in the 20th century, the development of antibiotics progressed rapidly. These drugs have been highly effective in preventing bacterial infections and protecting human health.[1] Tetracycline hydrochloride (TCH) and oxytetracycline hydrochloride (OTC) are two widely used tetracycline antibiotics in both the global livestock industry and the medical field.[2] TCH is resistant to degradation and can persist in aquatic and terrestrial environments for extended periods. Studies have shown that TCH may pose health risks, including joint lesions, endocrine disorders, kidney disease, and central nervous system defects.[3,4] Due to its high environmental mobility, the OTC has been detected in soil at concentrations of 300 μg kg^{-1} and in surface water at 15 μg L^{-1}.[5,6] The stability, toxicity, and bioaccumulation potential of the OTC classify it as a significant environmental pollutant.[7] Exposure to the OTC can alter microbial communities, affect gene transcription, and promote the proliferation of antibiotic-resistant genes, thereby increasing risks to human health.[8–10] To mitigate environmental pollution, it is imperative to develop effective methods for removing TCH and OTC from water bodies.

Various physical and chemical techniques have been explored for treating wastewater containing tetracyclines (TCs). These methods include electrocoagulation,[11] biodegradation,[12] membrane separation,[13] photocatalysis,[14] photodegradation,[15] advanced oxidation processes,[16] and adsorption.[17] Among these, adsorption is favored due to its operational simplicity, sustainability, cost-effectiveness, environmental friendliness, and the reusability of adsorbents, which reduces overall treatment costs.[18] Consequently, adsorption is considered the preferred method for removing organic pollutants from water.

Zero-valent iron (ZVI) effectively removes various pollutants, including chlorinated organic compounds,[19] heavy metal ions,[20] and antibiotics.[21–29] However, ZVI's reactivity decreases due to oxidation and agglomeration, which result from its large surface area. To address these issues, researchers have utilized porous materials such as zeolite, montmorillonite, clay, graphene oxide, and biochar (BC) to reduce nanoparticle aggregation.[30] Biochar, a carbon-rich substance produced by pyrolyzing biomass, is considered an excellent soil conditioner and a valuable tool for remediating contaminated waterways.[31] Its superior adsorption capabilities enable the effective removal of both organic and inorganic contaminants from water.[32] Tharindu N. *et al.* reported a composite material combining ZVI and renewable biomass obtained *via* pyrolytic reduction, which outperformed both ZVI nanoparticles and biochar derived from biomass when used independently as adsorbents.[20] Furthermore, the adsorption capacity of biochar can be enhanced through activation, with potassium hydroxide (KOH) commonly employed in the synthesis of activated biochar.[33]

[a]*School of Pharmacy, Guizhou Medical University, Guiyang, 561113, China*
[b]*Key Laboratory of Mountain Information System and Ecological Environment Protection, Guizhou Normal University, Guiyang, 550025, China*
† Xingzhi Yang and Xichang Wu are co-first-authors and contributed equally to this paper.

Camellia oleifera, a species within the genus *Camellia* of the family Theaceae, is widely cultivated in China. In 2023, the cultivated area dedicated *Camellia oleifera* to cultivating China encompassed roughly 4.67 covered approximately projections indicate an expansion estimate this will expand million hectares by the year 2025.[34] Processing quantity of *Camellia* volume generates substantial shell waste, leading to resource which contributes and environmental concerns. More importantly *Camellia oleifera* shells are rich in lignin and carbon, making them a valuable feedstock producing carbon-based functional materials.[35,36] Meanwhile, through the pyrolysis of oil tea shells, the M^{n+} bound within is reduced to zero-valent metal, which is a potential method for preparing zero-valent metal-loaded biochar for pollutant removal.

Therefore, we investigated the pyrolysis of tea tree shells to reduce Fe, Zn, and Co metal salts in order to prepare modified biochar for the removal of TCH and OTC from simulated wastewater. The adsorption test indicated that BC-600, which was loaded with zero-valent metal, shows the best adsorption capacity for TCH and OTC from simulated wastewater. Various characterization techniques were employed to analyze and investigate the structural morphology and adsorption mechanisms of BC-600. Adsorption kinetics and isotherm models were applied to analyze the experimental data and gain a deeper understanding of the adsorption mechanism. In addition, the effects of the solution concentration, pH, operating temperature, and the number of repeated experiments on the adsorption efficiency were investigated.

2. Materials and methods

2.1 Preparation of biochar

Primitive biochar. Pyrolysis was carried out in a tube oven using 10 g dried oil tea powder as raw material. Temperatures increased by 5 °C min^{-1} to 500 °C and 600 °C, respectively, and were maintained for 2 h to produce biochar. Throughout the process, nitrogen gas is continuously supplied to maintain an anaerobic environment. The resulting biochar is then sieved through a 0.15 nm mesh.

Modified biochar. To achieve optimal adsorption performance of modified biochar for tetracycline antibiotics, we prepared nine different types of modified biochar. Herein, we provide the preparation details for zero-valent iron-loaded biochar, which exhibits the highest capacity for antibiotic removal. The methods for preparing the other modified biochars are the same as those used for zero-valent iron-loaded biochar (Table S2). Briefly, 40 g of tea seed shells, 20 m mol of $FeCl_3 \cdot 6H_2O$, and 80 m mol of 2-methylimidazole ($C_4H_6N_2$) in 250 mL of deionized water. Stir the mixture for 24 h. After drying, place the mixture in a tube furnace. Heat it in stages (5 °C min^{-1}) until it reaches 600 °C. Maintain this temperature for 2 h to prepare the biochar. Dissolve the pyrolyzed biochar in water at a mass ratio of biochar to KOH to water of 1 : 2 : 20. Thoroughly stir the mixture and transfer it to a magnetic stirrer. Stir at 500 rpm and 25 °C for 24 h. After stirring, the mixture was vacuum-filtered and dried. Then, the dried biochar was subjected to a second pyrolysis under the same conditions as the initial process to ensure consistent temperatures and durations for both steps. The activated biochar was sieved through a 0.15 nm mesh screen. All modified biochar samples were labeled BCX-*Y*, where X represents the type and *Y* denotes the pyrolysis temperature.

2.2 Characterization of biochar

Scanning electron microscopy (Apreo 2, Thermo Fisher Scientific, USA) assessed raw and modified biochar morphology. Nitrogen adsorption–desorption isotherms (Microtrac Blue, TriStar II Plus, Microtrac, USA) determined surface area and pore characteristics. Thermogravimetric analysis (SDT Q 600, TA Instruments, USA) evaluated thermal stability up to 800 °C. FTIR (Nicolet iS10, Thermo Fisher Scientific, USA) identified functional group changes. XRD (SmartLab 9, Rigaku, Japan) analyzed crystalline phases. XPS (Escalab 250 Xi, Thermo Fisher Scientific, USA) examined elemental composition and oxidation states.

2.3 Adsorption experiments

First, a specified mass of the TCH and OTC was accurately weighed, dissolved, and made up to a 300 mg L^{-1} solution, followed by adjusting the pH to 4. Subsequently, combine 0.05 g of BC-600 with 30 mL of each TCH and OTC solution in 50 mL conical centrifuge tubes. Incubate the mixtures in a thermostatic water bath shaker at 25 °C for 90 min to facilitate reaction. Finally, filter out BC from the solutions and determine the concentrations of the TCH and OTC in the supernatant using UV-vis spectrophotometry (UV – 5500 PC, Shanghai Yuanxi Instrument Co., Ltd).

Adsorption kinetics. 0.05 g of BC were mixed with 300 mg L^{-1} solutions of the TCH and OTC and reacted in a thermostatic water bath shaker at 25 °C, with the solution pH adjusted to 4. The reaction times ranged from 10 to 360 min, with periodic measurements of the filtrate concentration.

Adsorption isotherms. Solutions of the TCH and OTC with concentrations ranging from 50 to 500 mol L^{-1} were prepared. Each solution was reacted with 0.05 g of BC at 25 °C for 90 min, maintaining the solution pH at 4.

Effect of operating temperature. The water bath temperature of the thermostatic shaker was set to 20, 25, 30, 35, 40, and 45 °C. Then, 0.05 g of BC was interacted with 300 mg L^{-1} TCH and OTC solutions (pH = 4) for 90 min, and the filtrate concentration was measured.

Effect of reaction temperature. The water bath temperature of the thermostatic shaker was set to 20, 25, 30, 35, 40, and 45 °C. Then, 0.05 g of BC was reacted with 300 mg L^{-1} TCH and OTC solutions (pH = 4) for 90 min, and the filtrate concentration was measured.

Reproducibility experiments. 0.10 g of BC was reacted with TCH and OTC solutions, followed by filtration and concentration measurement. The filtered BC was statically adsorbed in the desorption solution (1 mol L^{-1} NaOH) for 2 h. After filtration, BC was dried in an oven and re-reacted with TCH and OTC solutions. This process was repeated five times.

In each experimental iteration, the antibiotic samples were concurrently prepared without biochar or antibiotic compounds. No measurable variation in the antibiotic concentration was observed during the control trials. All adsorption experiments were conducted in triplicate.

2.4 Data analysis

The adsorption capacity and removal efficiency were calculated using eqn (1) and (2):[37]

$$Q_e = \frac{(C_0 - C)V}{m} \quad (1)$$

$$R = \frac{C_0 - C}{C_0} \times 100\% \quad (2)$$

where Q_e represents the adsorption capacity (mg g^{-1}); R denotes the removal rate; C_0 signifies the initial concentration (mg L^{-1}); C is the remaining concentration after biochar adsorption (mg L^{-1}); V is the solution volume; and m represents the biochar dosage (g).

The Langmuir (eqn (3)), Freundlich (eqn (4)) adsorption models were used to fit the adsorption isotherm data.

$$Q_e = \frac{K_L C_e q_{max}}{1 + K_L C_e} \quad (3)$$

$$Q_e = K_F C_e^{1/n} \quad (4)$$

where Q_e represents the adsorption capacity at equilibrium (mg g^{-1}); C_e denotes the concentration of the adsorbate in the solution at equilibrium (mg L^{-1}); K_L (mg g^{-1}) is the Langmuir constant; K_F (mg g^{-1}) is the Freundlich constant; q_{max} (mg g^{-1}) is the sorption capacity; and n signifies the adsorption intensity.

The quasi first-order kinetic model eqn (5) and the quasi second-order kinetic model eqn (6).

$$Q_t = Q_e(1 - e^{-K_1 t}) \quad (5)$$

$$\frac{t}{Q_e} = \frac{1}{K_2 \times Q_e^2} + \frac{t}{Q_e} \quad (6)$$

where Q_t (mg g^{-1}) represents the adsorption amount at time t (min); Q_e (mg g^{-1}) is the adsorption amount when equilibrium is reached; K_1 (min^{-1}) is the rate constant for the first-order kinetics, and K_2 (g mg^{-1} min^{-1}) is the rate constant for the second-order kinetics.

Thermodynamic analysis can be used to explore the trend of the biochar adsorption process eqn (7)–(9). The thermodynamic related formula is as follows.[26]

$$\Delta G^\circ = -RT \ln k_0 \quad (7)$$

$$\Delta G^\circ = \Delta H^\circ - T\Delta S^\circ \quad (8)$$

$$\ln k_0 = \frac{\Delta S^\circ}{R} - \frac{\Delta H^\circ}{RT} \quad (9)$$

where ΔG° (kJ mol^{-1}) is the standard Gibbs free energy; ΔH° (kJ mol^{-1}) is the standard enthalpy change; ΔS° (J mol^{-1} K^{-1}) is the standard entropy change; R is the gas constant, the value is 8.314 J mol^{-1} K^{-1}; k_0 is the adsorption equilibrium constant (Q_e/C_e).

3. Results and discussion

3.1 Biochar characteristics

SEM was used to analyze the surface morphology of biochar, allowing for a thorough analysis of structural changes after modification. Refer to Fig. 1a and b for the illustration, the surface of tea husk BC pyrolyzed at 600 °C exhibited a textured structure devoid of discernible pore structures, accompanied by surface collapse and the adhesion of irregularly shaped, blocky structures. Notably, the adsorption test indicates that only the

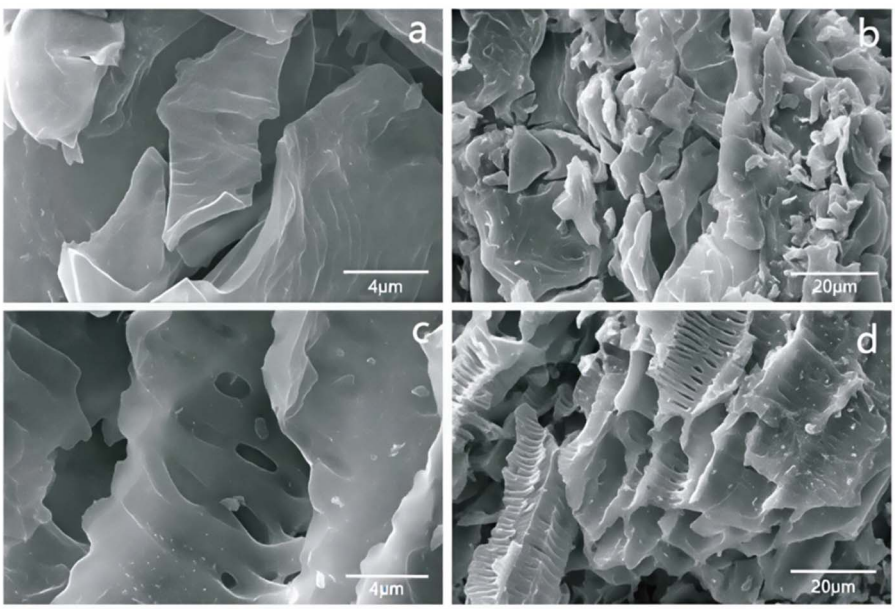

Fig. 1 SEM images of BC (a and b) and BC-600 (c and d).

biochar treated with $FeCl_3 \cdot 6H_2O$, $C_4H_6N_2$, and KOH exhibits the highest capacity for antibiotic removal. Therefore, only the BC-600 sample was investigated for its structure and morphology. As show in Fig. 1c and d, BC-600 showed a complex morphology, with distinct holes, irregular protrusions and depressions, and microscopic particles on the surface. It was particularly characterized by porous, stratified, or grid-like characteristics. This might be explained by the etching action of KOH as well as the effective addition of Fe, N, and K to BC, which stabilized its structure. The structure of the BC-600 adsorbent antibiotic remains unchanged, demonstrating excellent stability (Fig. S2).

The BET specific surface area and pore size distribution of BC and BC-600 were characterized *via* N_2 adsorption–desorption isotherms (Fig. 2). Both materials exhibit IV-type isotherms with pronounced hysteresis loops, which indicates the presence of mesoporous structures.[38] The surface area, pore volume, and average pore diameter are presented in Table 1. As shown, the BET surface areas of BC-600 and BC are 4.51 and 4.13 $m^2\ g^{-1}$, respectively. The total pore volumes were 0.0063 and 0.0016 $cm^3\ g^{-1}$, with average pore diameters of 5.27 and 4.70 nm. Compared with BC, BC-600 exhibits enhanced textural properties across these parameters.

Fig. 3a illustrates the variation in the mass of BC-600 as the temperature increases during thermogravimetric analysis. During the 0 to 150 °C range, the mass decreases by approximately 5.00%, attributable to the evaporation of residual moisture and minor volatile compounds within the biochar. Beyond 150 °C, the mass reduction stabilizes at 90.81%. As pyrolysis temperature continues to rise, the mass decline becomes more gradual, with a further reduction of only 5.13% between 150 °C and 650 °C, primarily due to the thermal decomposition of hemicellulose and cellulose in the biochar. From 650 to 800 °C, the rate of mass loss accelerates, culminating in a residual mass of 80.69% at 800 °C, representing an overall decrease of 19.31%.

Analysis by FTIR spectroscopy indicates the structure of the functional groups in biochar (BC-600) prior to the adsorption of the TCH and OTC (Fig. 3b). The BC sample exhibits –OH stretching vibration peaks at 3430, 1254, and 570 cm^{-1},[39,40] and C–H stretching vibration peaks are observed at 2917, 876, and 831 cm^{-1}.[41–43] Additionally, a C=C stretching vibration peak was detected at 1579 cm^{-1}.[44] The peak near 1100 cm^{-1} is attributed to C–O–C vibrations of ether, ester, or acid anhydride groups.[45] After modification, the C–H stretching vibration peak shifted from 2917 cm^{-1} to 2929 cm^{-1},[46,47] and the –OH peak at 1254 cm^{-1} disappeared. This may be due to a reaction between the –OH and Fe^{3+} in the modifying reagent. The other functional groups remained unchanged.

Table 1 Physical properties of BC and BC-600

Biochar	BET ($m^2\ g^{-1}$)	Total pore volume ($cm^3\ g^{-1}$)	Mean pore size (nm)
BC	4.13	0.0016	4.70
BC-600	4.51	0.0063	5.27

XRD analysis was utilized for the identification of crystalline phases, relying on the diffraction patterns of X-rays, specifically the position, intensity, and quantity of diffraction lines.[48] As illustrated in Fig. 3c, graphitic carbon was detected in the biochar BC, pyrolyzed at 600 °C, with a characteristic peak at 26.2°. Following the modification, the BC-600 samples displayed the distinctive peaks of ZVI at $2\theta = 44.7°$ and 65.0° (PDF # 98-000-0259), which suggests the successful reduction of Fe^{3+} to ZVI under a nitrogen atmosphere.[49]

Fig. 3d shows the XPS spectra and peak shapes of BC, BC-600, BC-600-TCH, and BC-600-OTC before and after adsorption of the TCH and OTC. Fig. 3d indicates that after TCH and OTC adsorption, the BC-600 sample exhibits C 1s, O 1s, N 1s, K 2p, and Fe 2p peaks, a finding confirmed by spectral analysis. The K 2p peak was not prominent after TCH and OTC adsorption, possibly due to coordination interactions between K^+ and antibiotics during adsorption.

Fig. 11 shows that the C 1s peaks at 284.8 eV, 285.9 eV and 288.9 eV correspond to C–C, C–O–C and O–C=O bonds respectively. The O 1s peaks at 533.2 eV, 530.9 eV, and 531.5 eV correspond to –COOH, C–OH, and O–H, respectively.[50–52] The Fe 2p peaks at 713.2 eV, 710.6 eV and 706.5 eV correspond to Fe^{3+}, Fe^{2+} and Fe^0, respectively.[53,54]

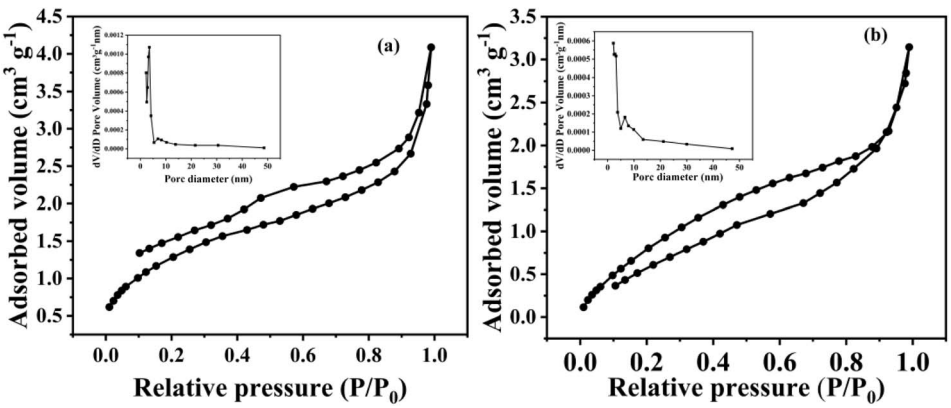

Fig. 2 N_2 adsorption–desorption isotherms of BC-600 (a) and BC (b).

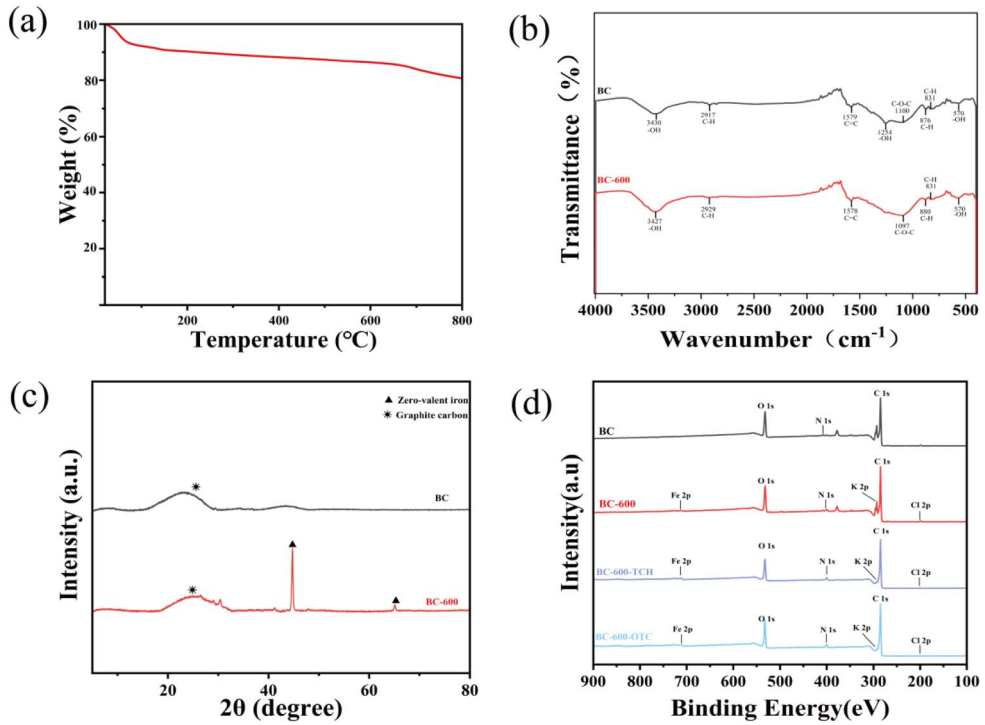

Fig. 3 Thermogravimetric analysis of BC-600 (a). FTIR (b) and XRD (c) for BC and BC-600. XPS spectra of BC, BC-600, BC-600-OTC and BC-600-TCH (d).

3.2 Adsorption performance of biochar

Fig. 4a and b show the adsorption kinetic curves for the TCH and OTC, respectively. These figures reveal how these two antibiotics are adsorbed onto biochar. The TCH initially exhibits a rapid upward trend (Fig. 4a), followed by a gradual slowdown in the adsorption rate. This initial rapid adsorption phenomenon is primarily due to the biochar's abundant microporous and mesoporous structures, as well as its large number of surface functional groups during the early adsorption stage. These surface functional groups provide multiple active adsorption sites that facilitate the rapid attachment and enrichment of pollutant molecules or ions through mechanisms such as electrostatic adsorption, hydrogen bonding, and π–π interactions. As the adsorption process progresses, the number of available active sites decreases, leading to a decline in the adsorption rate. At this point, the surface reaches a saturated state. Additionally, the significant antibiotic concentration gradient between the internal pore structure of the biochar and the surrounding aqueous phase enhances the driving forces of mass transfer, accelerating the diffusion of tetracycline molecules and their occupation of adsorption sites. Fig. 4b shows that the adsorption capacity stabilizes after approximately 30 min, with subsequent adsorption quantities remaining relatively constant. This indicates that adsorption equilibrium has been established. This steady state indicates that the rates of adsorption and desorption are equal,

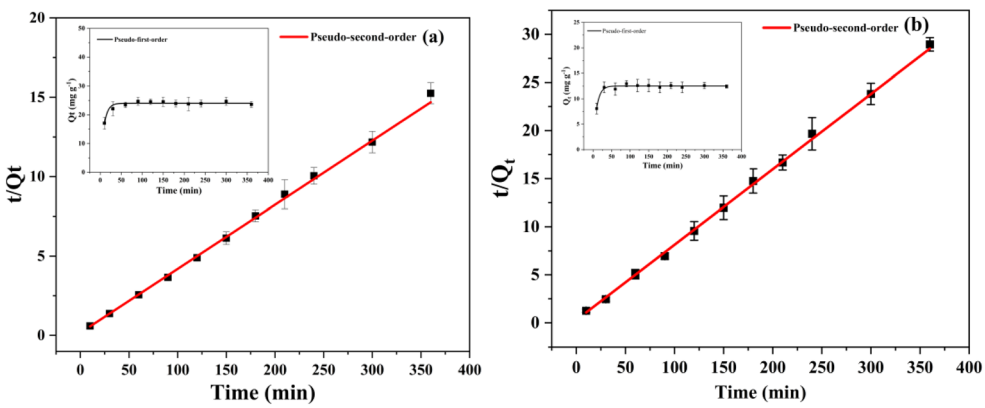

Fig. 4 Adsorption kinetics of the TCH (a) and OTC (b) by BC-600.

Table 2 Adsorption kinetic parameters of the TCH and OTC by BC-600

		Pseudo-first-order kinetics			Pseudo-second-order kinetics		
Biochar	Adsorbates	Q_e (mg g^{-1})	K_1	R^2	Q_e (mg g^{-1})	K_2	R^2
BC-600	TCH	24.04	0.119	0.869	24.77	0.010	0.999
	OTC	12.53	0.105	0.940	12.76	0.021	0.998

representing dynamic equilibrium under experimental conditions and the maximum adsorption capacity of biochar for antibiotics.

As shown in Table 2, the R^2 values for the pseudo-first-order and the pseudo-second-order kinetic models for the TCH adsorption are 0.869 and 0.999, respectively. For the OTC adsorption, the R^2 values are 0.940 and 0.998, respectively. The TCH and OTC adsorption processes by BC-600 can be well described by the pseudo-second-order kinetic model. This suggests that the adsorption mechanisms of these two antibiotics primarily involve chemical adsorption. The Q_e value for the TCH (24.77 mg g^{-1}) is higher than that for the OTC (12.76 mg g^{-1}), suggesting that the TCH exhibited a stronger affinity for BC-600.

This study employed BC-600 biochar as an adsorbent to investigate the adsorption performance of the TCH and OTC solutions at varying concentrations. Fig. 5 presents the analytical results, with the experimental data fitted to both the Langmuir and Freundlich adsorption models. As the equilibrium concentration (C_e) of antibiotics increased, the adsorption capacity of BC-600 for both antibiotics also enhanced, indicating the material's efficacy in adsorbing pollutants across varying concentrations. The model fitting results in Table 3 reveal that, when comparing the Langmuir R^2 values (0.926, 0.969) with the Freundlich R^2 values (0.990, 0.983), the Freundlich model better describes the adsorption of the TCH and OTC onto BC-600. This indicates that BC-600 exhibits multi-layer, heterogeneous surface adsorption phenomena for both antibiotics. The n-value represents the adsorption strength: both the TCH and OTC exhibit n-values greater than 1, indicating effective adsorption capacity. The $1/n$ values reflect affinity: those for the TCH and OTC were 0.476 and 0.117 respectively, falling within the 0.1 to 0.5 range, indicating strong affinity during adsorption. According to the formula $R_L = 1/(1 + K_L \times C_0)$, when $0 < R_L < 1$, the adsorption process is favorable. For the adsorption experiments of the TCH and OTC, the R_L values were 0.0020 and 0.0018 respectively, indicating a significantly advantageous adsorption process.

Fig. 6 shows the adsorption kinetics of the TCH and OTC on the biochar composite material BC-600. The pH of the solution was adjusted from 2 to 7 to investigate this phenomenon. The TCH adsorption efficiency exhibited a biphasic trend: initial increase, followed by a decrease, then a subsequent increase, with significant fluctuations between pH 2–3 and 3–4. When the pH was between 5 and 7, the adsorption performance stabilized. The OTC adsorption curve initially increased, then decreased,

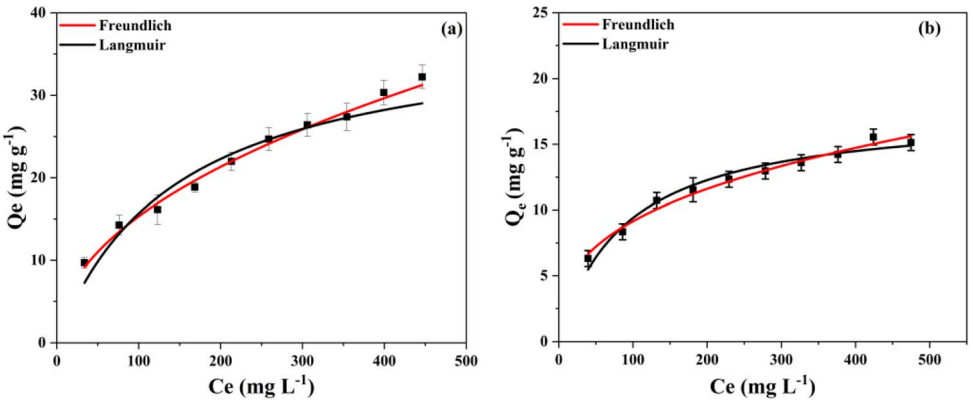

Fig. 5 Adsorption isotherms of the TCH (a) and OTC (b) by BC-60.

Table 3 Adsorption isotherm parameters of BC-600 for the TCH and OTC

		Langmuir model			Freundlich model			
Biochar	Adsorbates	q_{max} (mg g^{-1})	K_L	R^2	n	K_F	R^2	$1/n$
BC-600	TCH	38.53	0.007	0.926	2.097	1.704	0.990	0.476
	OTC	17.66	0.011	0.969	2.915	1.885	0.983	0.117

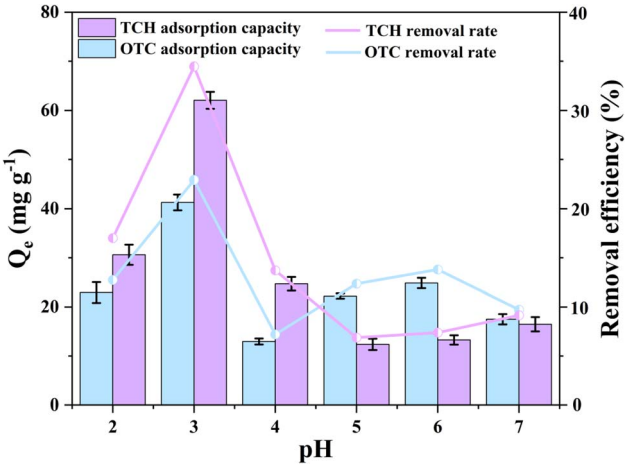

Fig. 6 Effect of pH on the adsorption of the TCH and OTC by BC-600.

increased again, and finally decreased. Between pH 2 and 4, its adsorption behavior resembled that of the TCH: the adsorption capacity increased from 12.96 mg g^{-1} to 24.85 mg g^{-1} and then decreased to 17.51 mg g^{-1} when the pH was neutral. Overall, pH significantly influences the adsorption of the TCH and OTC on BC. The optimum pH is 3, with the TCH exhibiting a maximum adsorption capacity of 62.07 mg g^{-1}, while the OTC demonstrates a maximum adsorption capacity of 41.28 mg g^{-1}.

This study examined how adjusting the amount of adsorbent BC-600 affects the adsorption capacity. As Fig. 7 shows, there is a clear inverse relationship between adsorption capacity and dosage of the adsorbent. Active sites are the core elements that regulate the adsorption mechanism. Specifically, increasing the dosage of the adsorbent can enhance the total number of effective active sites, thereby improving the overall adsorption efficiency. However, as the sites become saturated, adsorption capacity decreases. Under constant antibiotic concentration conditions, an excess of active sites leads to competition for adsorption among adsorbate molecules. This reduces the utilization efficiency of each site, ultimately resulting in

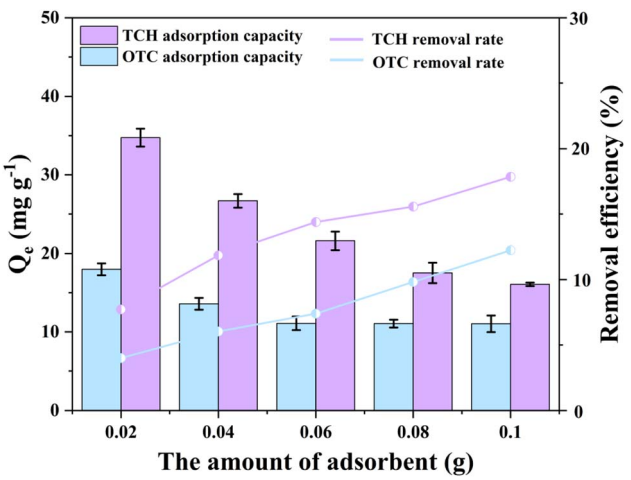

Fig. 7 Effect of the adsorbent dosage.

Table 4 Comparison of the adsorption capacities of the reported sorbents for the tetracycline antibiotics

Sorbents	Capacities of antibiotics (mg g^{-1})		Ref.
	TC	OTC	
ZVI@biochar	52.7	39.1	Hao *et al.*[55]
ZVI@ACCS nanocomposites	78.3	66.8	Song *et al.*[56]
565RCL-nZVI	72.4	—	Ahmed M. *et al.*[57]
nZVI-HBC	—	196.7	Li *et al.*[58]
PnZVI/ESBC	304.6	—	Huang *et al.*[59]
BC/S/Fe^0	505.6	—	Yang *et al.*[60]
BC	4.9	3.2	This work
BC-600	62.0	41.2	This work

a decrease in the adsorption capacity. Furthermore, weakened concentration gradients and increased steric hindrance hinder the diffusion of adsorbate molecules, further reducing the adsorption efficiency. The sorbent's adsorption capacity is compared to that of the other sorbents in Table 4.

The adsorption capacity of biochar for the TCH and OTC is influenced not only by pH and dosage, but also by reaction temperature. This study systematically analyzes how temperature changes impact the adsorption of the TCH and OTC in biochar, using the thermodynamic parameters presented in Fig. 8 and Table 5. As the temperature rises from 20 °C to 45 °C, the adsorption capacity decreases sharply, dropping from 26.81 mg g^{-1} at 20 °C to 12.22 mg g^{-1} (TCH). Correspondingly, the removal efficiency drops from 14.00% to 12.85%, a 8.11% decrease.

According to Table 5, the enthalpy change of the TCH adsorption reaction ($\Delta H^\circ < 0$) is negative, indicating that it is exothermic. However, the Gibbs free energy change is positive ($\Delta G^\circ > 0$), meaning that the process is non-spontaneous within this temperature range. Therefore, an increase in the temperature inhibits the TCH adsorption. The OTC adsorption process

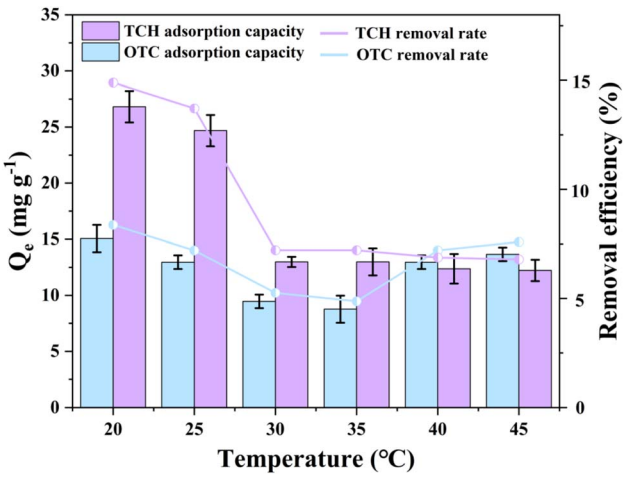

Fig. 8 Effect of reaction temperature on the adsorption of the TCH and OTC by BC-600.

Table 5 Thermodynamic parameters of the TCH and OTC by BC-600

Biochar	Adsorbates	Temperature (K)	k_0	$\Delta G°$ (kJ mol^{-1})	$\Delta H°$ (kJ mol^{-1})	$\Delta S°$ (J mol^{-1} K^{-1})	R^2
BC-600	TCH	293	0.105	5.490	−29.871	−121.38	0.769
		298	0.095	5.822			
		303	0.047	7.722			
		308	0.047	7.850			
		313	0.044	8.120			
		318	0.044	8.276			
	OTC	293	0.055	7.075	−31.108	−130.28	0.954
		298	0.047	7.599			
		303	0.033	8.571			
		308	0.031	8.919			
		308	0.031	8.919	38.642	96.98	0.854
		313	0.047	7.981			
		318	0.049	7.959			

can be divided into two stages. In the first stage (20 to 35 °C), the adsorption capacity and removal efficiency of BC for the OTC decreased as the temperature increases: by 6.29 mg g^{-1} and 3.50%, respectively. Thermodynamic analysis showed that the $\Delta H°$ value remains negative while the $\Delta G°$ value is positive. This confirms that the process is a non-spontaneous exothermic reaction. Thus, an increase in temperature is unfavorable for the OTC adsorption. In the second stage (35 to 45 °C), the adsorption capacity and removal efficiency increased by 4.89 mg g^{-1} and 2.72%, respectively. Thermodynamic data indicate that both $\Delta H°$ and $\Delta G°$ are positive within this temperature range, suggesting that the process is a non-spontaneous endothermic reaction.[61] Therefore, elevating the temperature during this phase can enhance the OTC adsorption, leading to improved removal efficiency.

Fig. 9 shows that the cyclic adsorption–desorption performance of BC-600 for the TCH and OTC exhibited significant fluctuations during the first three operational cycles. The removal efficiencies of the two antibiotics decreased by 6.84% and 6.80%, respectively, indicating a weakened adsorption effectiveness in the early stages. However, from the fourth to the fifth cycle, the adsorption capacity of the TCH and OTC stabilized, approaching equilibrium. This indicates that the adsorbent performance partially recovered or stabilized. After five cycles, the quantitative analysis showed that the adsorption capacity of the TCH decreased from 16.07 to 7.48 mg g^{-1} and the removal rate decreased from 17.85 to 8.31%. Similarly, the adsorption capacity of the OTC decreased from 11.03 to 3.33 mg g^{-1}, and the removal efficiency decreased from 12.25 to 3.70%. This decline in adsorption performance with an increasing number of cycles is likely due to the gradual depletion of the surface functional groups and active adsorption sites on the BC material. This depletion stems from repeated use and regeneration processes, thereby reducing the material's overall pollutant removal efficiency. After five adsorption cycles of the TCH and OTC, the iron ion leaching rate of BC-600 (Fig. S3) was significantly below the EU discharge standard (2 mg L^{-1}).[62]

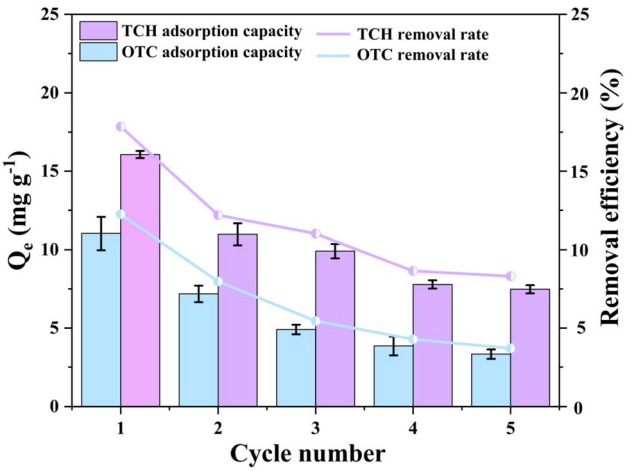

Fig. 9 Reusability performance of BC-600.

3.3 Adsorption mechanism

Fig. 10 displays the FTIR and XRD spectra of BC-600 before and after adsorption of the TCH and OTC. As shown in Fig. 10a, following the TCH adsorption, the C–H stretching vibration peak at 2917 cm^{-1} in the BC-600-TCH sample disappears, while the C–H peak at 831 cm^{-1} shifts to 805 cm^{-1}. Similarly, following the OTC adsorption, the C–H peak in the BC-600-OTC sample shifted from 831 cm^{-1} to 803 cm^{-1}, whilst other functional groups remained stable. Following adsorption of the TCH (3433 cm^{-1}) and OTC (3435 cm^{-1}), the –OH stretching vibration peak (3427 cm^{-1}) shifted and intensified. This indicates hydrogen bonding interactions between BC-600 and the antibiotics.[31] As shown in Fig. 10b, the adsorption of antibiotics caused the ZVI absorption peak to weaken, demonstrating the involvement of ZVI in the adsorption process.

Fig. 11 shows the XPS spectra of BC-600 absorbing the TCH and OTC. Following adsorption, shifts in the C–H and –OH peaks indicate the presence of π–π stacking and hydrogen bonding interactions. The O–C=O bond transforms into a C–C bond, as evidenced by the marked reduction in the O–C=O peak area. This suggests that oxygen-containing functional groups participate in the desorption mechanism *via* π–π

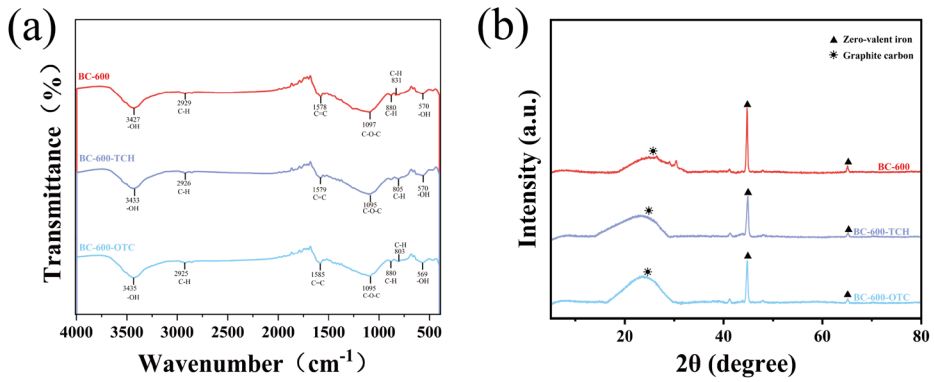

Fig. 10 FTIR (a) and XRD (b) of BC-600 before and after adsorption of the TCH and OTC.

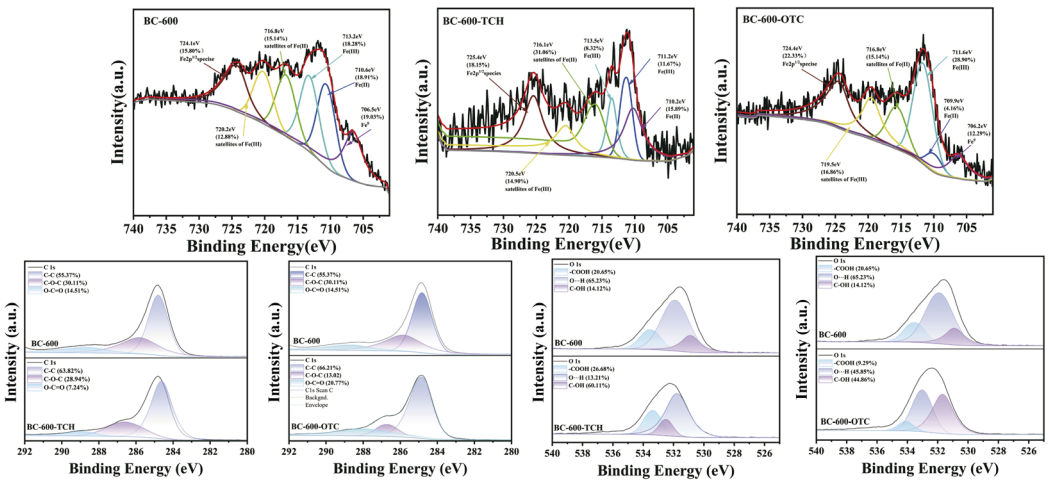

Fig. 11 XPS peak diagram before and after adsorption of the TCH and OTC by BC-600.

stacking interactions.[63] The decrease in the O–H peak area after adsorption indicates that hydrogen bonding plays a significant role in the adsorption of the TCH and OTC. The increase in the C–C and C–OH peak areas may be attributed to BC-600 successfully adsorbing the antibiotics. These findings are corroborated by FTIR results. Compared to pre-adsorption, the Fe^0 peak area decreased. ZVI acts as a reducing agent and can be oxidised by water and dissolved oxygen in solution to form ferrous and ferric ions. These ions can then form stable complexes with the phenolic β-diketone structure of the TC group. Following ZVI corrosion, hydrated iron oxide forms on its surface. Through surface complexation between this hydrated iron oxide and the TC groups, the binding sites for antibiotics become more active.[56] Consequently, hydrogen bonding, π–π stacking and electrostatic interactions are involved in the adsorption of antibiotics by BC-600.

Two tetracycline antibiotics and pH-dependent charge regulation on the biochar surface jointly govern electrostatic interactions during adsorption.[64] The zero-charge point (pH_{ZPC}) of BC-600 was determined at pH = 3.17 (Fig. S4), with the zeta potential exhibiting a negative correlation with pH. Both antibiotics exist as cations at pH < 3.3 and as zwitterions at pH 3.3–7.68. When pH < 3, both the BC-600 surface and antibiotics carry strong positive charges, inducing intense electrostatic repulsion that reduces the adsorption capacity, whereas at pH > 3, the BC-600 surface carries negative charge, causing the zeta potential to gradually decrease. Antibiotics simultaneously carry both positive and negative charges, and their charge distribution alters with pH changes. Initially, electrostatic repulsion weakens, leading to a corresponding increase in adsorption capacity, but subsequently strengthens again. Thus, electrostatic interactions play a crucial role in the adsorption process.[65–68]

4. Conclusion

This study successfully loaded ZVI onto BC (BC-600) and investigated the adsorption performance of BC-600 towards TCs in aqueous solutions. The effects of pH, initial contaminant concentration, contact time, and adsorbent dosage on the removal efficiency of pharmaceutical pollutants were examined. The synthesised composite material demonstrated favourable adsorption performance towards TCs. The mechanism governing BC-600's removal of tetracycline is controlled by

electrostatic interactions, hydrogen bonding, and π–π interactions between the drug molecules and the adsorbent. Analysis of the adsorption isotherm and kinetic data indicates that the adsorption process conforms to the Freundlich model and pseudo-second-order kinetic model, with corresponding correlation coefficients. Studies on tetracycline removal in aqueous media indicate a maximum adsorption capacity of 62.07 mg g^{-1} (TCH) and 41.28 mg g^{-1} (OTC) at the optimum pH of 3. Difficulties in desorption during cycling resulted in suboptimal performance. Given its suitable adsorption capacity and environmentally benign properties, BC-600 represents an acceptable and suitable adsorbent for removing pharmaceutical contaminants from wastewater.

Conflicts of interest

There are no conflicts of interest to declare.

Data availability

The authors confirm that the data supporting the findings of this study are available within the article and its supplementary information (SI). Supplementary information is available. See DOI: https://doi.org/10.1039/d5ra04362j.

Acknowledgements

This work is supported by the project of Guizhou Provincial Department of Science and Technology (Qian Ke He Jichu-ZK [2024] zhong dian 055, Qiankehe Zhicheng [2023] 078), and Projects of Forestry Research in Guizhou Province (GUI[2022] TSLY07).

References

1 S. Eslaminejad, R. Rahimi and M. Fayazi, Green decoration of Pd nanoparticles on MXene/metal organic framework support for photocatalytic degradation of ofloxacin, *J. Ind. Eng. Chem.*, 2025, **141**, 94–103, DOI: 10.1016/j.jiec.2024.06.020.

2 Y. Wu, H. Cheng, D. Pan, *et al.*, Potassium hydroxide-modified algae-based biochar for the removal of sulfamethoxazole: sorption performance and mechanisms, *J. Environ. Manag.*, 2021, **293**, 112912, DOI: 10.1016/j.jenvman.2021.112912.

3 J. Leichtweis, Y. Vieira, N. Welter, *et al.*, A review of the occurrence, disposal, determination, toxicity and remediation technologies of the tetracycline antibiotic, *Process Saf. Environ. Prot.*, 2022, **160**, 25–40, DOI: 10.1016/j.psep.2022.01.085.

4 Y. Ni, J. Yang, L. Sun, *et al.*, La/LaF3 co-modified MIL-53(Cr) as an efficient adsorbent for the removal of tetracycline, *J. Hazard. Mater.*, 2022, **426**, 128112, DOI: 10.1016/j.jhazmat.2021.128112.

5 D. L. Makoff, Chronic calcium carbonate therapy in uremia, *Arch. Intern. Med.*, 1969, **123**(1), 15–21, DOI: 10.1001/archinte.123.1.15.

6 D. Fatta-Kassinos, S. Meriç and A. Nikolaou, Pharmaceutical residues in environmental waters and wastewater: current state of knowledge and future research, *Anal. Bioanal. Chem.*, 2010, **399**(1), 251–275, DOI: 10.1007/s00216-010-4300-9.

7 J.-A. Park, M. Pineda, M.-L. Peyot, *et al.*, Degradation of oxytetracycline and doxycycline by ozonation: degradation pathways and toxicity assessment, *Sci. Total Environ.*, 2023, **856**, 159076, DOI: 10.1016/j.scitotenv.2022.159076.

8 H. Zhang, S. Xue, J. Zhang, *et al.*, Performance and mechanism of sycamore flock based biochar in removing oxytetracycline hydrochloride, *Bioresour. Technol.*, 2022, **350**, 126884, DOI: 10.1016/j.biortech.2022.126884.

9 N. Li, L. Zhou, X. Jin, *et al.*, Simultaneous removal of tetracycline and oxytetracycline antibiotics from wastewater using a ZIF-8 metal organic-framework, *J. Hazard Mater.*, 2019, **366**, 563–572, DOI: 10.1016/j.jhazmat.2018.12.047.

10 N. Li, L. Zhang, X. Jin, *et al.*, Simultaneous removal of tetracycline and oxytetracycline antibiotics from wastewater using a ZIF-8 metal organic-framework, *J. Hazard. Mater.*, 2019, **366**, 563–572, DOI: 10.1016/j.jhazmat.2018.12.047.

11 P. Mandal, O. Lanaridi, B. Warth, *et al.*, Metabolomics as an emerging approach for deciphering the biological impact and toxicity of food contaminants: the case of mycotoxins, *Crit. Rev. Food Sci. Nutr.*, 2023, 1–25, DOI: 10.1080/10408398.2023.2217451.

12 H.-R. Zuo, P. Shi and M. Duan, A review on thermally stable membranes for water treatment: material, fabrication, and application, *Sep. Purif. Technol.*, 2020, **236**, 116223, DOI: 10.1016/j.seppur.2019.116223.

13 S. Riaz and S.-J. Park, An overview of TiO2-based photocatalytic membrane reactors for water and wastewater treatments, *J. Ind. Eng. Chem.*, 2020, **84**, 23–41, DOI: 10.1016/j.jiec.2019.12.021.

14 D. Ayodhya and G. Veerabhadram, A review on recent advances in photodegradation of dyes using doped and heterojunction based semiconductor metal sulfide nanostructures for environmental protection, *Mater. Today Energy*, 2018, **9**, 83–113, DOI: 10.1016/j.mtener.2018.05.007.

15 M. M. M'Arimi, C. A. Mecha, A. Kiprop, *et al.*, Recent trends in applications of advanced oxidation processes (AOPs) in bioenergy production: review, *Renewable Sustainable Energy Rev.*, 2020, **121**, 109669, DOI: 10.1016/j.rser.2019.109669.

16 J. Wang, R. Zhuan and L. Chu, The occurrence, distribution and degradation of antibiotics by ionizing radiation: an overview, *Sci. Total Environ.*, 2019, **646**, 1385–1397, DOI: 10.1016/j.scitotenv.2018.07.415.

17 S. De Gisi, G. Lofrano, M. Grassi, *et al.*, Characteristics and adsorption capacities of low-cost sorbents for wastewater treatment: a review, *Sustain. Mater. Technol.*, 2016, **9**, 10–40, DOI: 10.1016/j.susmat.2016.06.002.

18 X. Chen, X. Jiang, Y. Chen, *et al.*, Facile fabrication of hierarchical porous ZIF-8 for enhanced adsorption of antibiotics, *J. Hazard. Mater.*, 2019, **367**, 194–204, DOI: 10.1016/j.jhazmat.2018.12.080.

19 S. Cai, Z. Cao, L. Yang, *et al.*, Cations facilitate sulfidation of zero-valent iron by elemental sulfur: mechanism and dechlorination application, *Water Res.*, 2023, **242**, 120262, DOI: 10.1016/j.watres.2023.120262.

20 T. N. Karunaratne, R. M. O. Nayanathara, C. Navarathna, *et al.*, Pyrolytic synthesis of graphene-encapsulated zero-valent iron nanoparticles supported on biochar for heavy metal removal, *Biochar*, 2022, **4**, 1–17, DOI: **10.1007/s42773-022-00196-5**.

21 Y. Chai, F. Wang and Y. Gao, Ozone activation over core-shell nanoreactors for enhanced organic pollutants degradation: surface-bound superoxide radicals induced by confinement effect, *Environ. Res.*, 2025, **282**, 122099, DOI: **10.1016/j.envres.2025.122099**.

22 M. B. Ahmed, J. L. Zhou, H. H. Ngo, *et al.*, Nano-Fe 0 immobilized onto functionalized biochar gaining excellent stability during sorption and reduction of chloramphenicol via transforming to reusable magnetic composite, *Chem. Eng. J.*, 2017, **322**, 571–581, DOI: **10.1016/j.cej.2017.04.063**.

23 W. Xue, X. Shi, J. Guo, *et al.*, Affecting factors and mechanism of removing antibiotics and antibiotic resistance genes by nano zero-valent iron (nZVI) and modified nZVI: a critical review, *Water Res.*, 2024, **253**, 121309, DOI: **10.1016/j.watres.2024.121309**.

24 A. Wang, J. Hou, Y. Feng, J. Wu and L. Miao, Removal of tetracycline by biochar-supported biogenetic sulfidated zero valent iron: kinetics, pathways and mechanism, *Water Res.*, 2022, **225**, 119168, DOI: **10.1016/j.watres.2022.119168**.

25 Z. Tang, Y. Kong, Y. Qin, *et al.*, Performance and degradation pathway of florfenicol antibiotic by nitrogen-doped biochar supported zero-valent iron and zero-valent copper: a combined experimental and DFT study, *J. Hazard. Mater.*, 2023, **459**, 132172, DOI: **10.1016/j.jhazmat.2023.132172**.

26 S. Wang, M. Zhao, M. Zhou, *et al.*, Biochar-supported nZVI (nZVI/BC) for contaminant removal from soil and water: a critical review, *J. Hazard. Mater.*, 2019, **373**, 820–834, DOI: **10.1016/j.jhazmat.2019.03.080**.

27 M. Sun, Y. Ma, Y. Yang, *et al.*, Effect of iron impregnation ratio on the properties and adsorption of KOH activated biochar for removal of tetracycline and heavy metals, *Bioresour. Technol.*, 2023, **380**, 129081, DOI: **10.1016/j.biortech.2023.129081**.

28 C. Wang, H. Dai, L. Liang, *et al.*, Enhanced mechanism of copper doping in magnetic biochar for peroxymonosulfate activation and sulfamethoxazole degradation, *J. Hazard. Mater.*, 2023, **458**, 132002, DOI: **10.1016/j.jhazmat.2023.132002**.

29 N. Zhao, K. Liu, B. Yan, *et al.*, Chlortetracycline hydrochloride removal by different biochar/Fe composites: a comparative study, *J. Hazard. Mater.*, 2021, **403**, 123889, DOI: **10.1016/j.jhazmat.2020.123889**.

30 C. Jin, B. Han, C. Luo, *et al.*, Precise synthesis of Fe single-atom catalysts on montmorillonite/g-C3N4 heterostructures for highly efficient fenton-like degradation of organic pollutants, *Water Res.*, 2025, **287**, 124420, DOI: **10.1016/j.watres.2025.124420**.

31 M. Yang, X. Chen, D. Ai, *et al.*, Sulfur-doped zero-valent iron supported on biochar for tetracycline adsorption and removal, *J. Clean. Prod.*, 2022, **379**, 134769, DOI: **10.1016/j.jclepro.2022.134769**.

32 M. He, Z. Xu, D. Hou, *et al.*, Waste-derived biochar for water pollution control and sustainable development, *Nat. Rev. Earth Environ.*, 2022, **3**(7), 444–460, DOI: **10.1038/s43017-022-00306-8**.

33 C. Zhao, J. Ma, Z. Li, *et al.*, Highly enhanced adsorption performance of tetracycline antibiotics on KOH-activated biochar derived from reed plants, *RSC Adv.*, 2020, **10**(9), 5066–5076, DOI: **10.1039/c9ra09208k**.

34 H. Zhang, S. Xue, J. Zhang, *et al.*, Performance and mechanism of sycamore flock based biochar in removing oxytetracycline hydrochloride, *Bioresour. Technol.*, 2022, **350**, 126884, DOI: **10.1016/j.biortech.2022.126884**.

35 J. Ren, Y. Zhang, H. Wang, *et al.*, Adsorption of Dibenzofuran by Modified Biochar Derived from Microwave Gasification: Impact factors and adsorption mechanism, *J. Anal. Appl. Pyrolysis*, 2024, 106831, DOI: **10.1016/j.jaap.2024.106831**.

36 L. Zhou, Y. Peng, Z. Xu, *et al.*, The Antioxidant, Anti-Inflammatory and Moisturizing Effects of Camellia oleifera Oil and Its Potential Applications, *Molecules*, 2024, **29**(8), 1864, DOI: **10.3390/molecules29081864**.

37 K. Sun, J. Jiang and D. Cui, Preparation of activated carbon with highly developed mesoporous structure from Camellia oleifera shell through water vapor gasification and phosphoric acid modification, *Biomass Bioenergy*, 2011, **35**(8), 3643–3647, DOI: **10.1016/j.biombioe.2011.05.007**.

38 M. Fayazi, Removal of mercury(II) from wastewater using a new and effective composite: sulfur-coated magnetic carbon nanotubes, *Environ. Sci. Pollut. Res. Int.*, 2020, **27**(11), 12270–12279, DOI: **10.1007/s11356-020-07843-z**.

39 H. Li, C. Zhou, L. L. Wang, *et al.*, A novel eco-friendly bamboo-based composite biochar for effective removing oxytetracycline hydrochloride, *Adv. Compos. Hybrid Mater.*, 2025, **8**(1), 91, DOI: **10.1007/s42114-024-01186-w**.

40 H. Zhao, J. Wang, S. Li, *et al.*, Evaluation and optimization of six adsorbents for removal of tetracycline from swine wastewater: experiments and response surface analysis, *J. Environ. Manage.*, 2024, **368**, 122170, DOI: **10.1016/j.jenvman.2024.122170**.

41 W. Tongyu, X. Song, J. Zhang, *et al.*, Efficient adsorption of tetracycline hydrochloride by Willow Catkins based biochar: performance, governing factors and mechanisms, *Biomass Convers. Biorefin.*, 2024, **14**(16), 18761–18773, DOI: **10.1007/s13399-023-04146-4**.

42 T. Fu, S. Wu, M. Zhao, *et al.*, Preparation and application of cattail residue-based magnetic cellulose composites for tetracycline antibiotics adsorption, *Process Saf. Environ. Prot.*, 2024, **189**, 598–611, DOI: **10.1016/j.psep.2024.06.114**.

43 J. Wen, Y. Zhou, T. Liu, *et al.*, Efficient adsorption-photocatalytic performance of La2S3/MgO-modified biochar in the removal of tetracycline hydrochloride at a low optical density, *Mater. Sci. Semicond. Process.*, 2023, **165**, 107690, DOI: **10.1016/j.mssp.2023.107690**.

44 S. Nand, S. Kumar, B. Pratap, *et al.*, Arsenic removal using de-oiled mentha biomass biochar: adsorption kinetics and the role of iron modification, *J. Clean. Prod.*, 2024, **482**, 144247, DOI: **10.1016/j.jclepro.2024.144247**.

45 H. Zhao, J. Wang, S. Li, *et al.*, Evaluation and optimization of six adsorbents for removal of tetracycline from swine wastewater: experiments and response surface analysis, *J. Environ. Manage.*, 2024, **368**, 122170, DOI: 10.1016/j.jenvman.2024.122170.

46 F. Ma, H. Zhao, X. Zheng, *et al.*, Enhanced adsorption of cadmium from aqueous solution by amino modification biochar and its adsorption mechanism insight, *J. Environ. Chem. Eng.*, 2023, **11**(3), 109747, DOI: 10.1016/j.jece.2023.109747.

47 Y. Ma, R. Wang, C. Gao, *et al.*, Carbon nanotube-loaded copper-nickel ferrite activated persulfate system for adsorption and degradation of oxytetracycline hydrochloride, *J. Colloid Interface Sci.*, 2023, **640**, 761–774, DOI: 10.1016/j.jcis.2023.03.001.

48 Y. Liu, J. Li, L. Wu, *et al.*, Magnetic spent bleaching earth carbon (Mag-SBE@C) for efficient adsorption of tetracycline hydrochloride: response surface methodology for optimization and mechanism of action, *Sci. Total Environ.*, 2020, **722**, 137817, DOI: 10.1016/j.scitotenv.2020.137817.

49 D. Li, W. Gu, L. Zhou, *et al.*, From biochar to functions: lignin induced formation of Fe3C in carbon/Fe composites for efficient adsorption of tetracycline from wastewater, *Sep. Purif. Technol.*, 2023, **304**, 122217, DOI: 10.1016/j.seppur.2022.122217.

50 X. Li, T. Gan, J. Zhang, *et al.*, High-capacity removal of oxytetracycline hydrochloride from wastewater via Mikania micrantha Kunth-derived biochar modified by Zn/Fe-layered double hydroxide, *Bioresour. Technol.*, 2022, **361**, 127646, DOI: 10.1016/j.biortech.2022.127646.

51 X. Huang, F. Li, X. Zhang, *et al.*, One-step high-efficiency microwave synthesis of N-doped bamboo biochar for tetracycline degradation, *Sep. Purif. Technol.*, 2024, **354**, 129003, DOI: 10.1016/j.seppur.2024.129003.

52 Z. Huang, B. Chang, Y. Tang, *et al.*, Co-adsorption performance and mechanism of ammonium and phosphate by iron-modified biochar in water, *J. Water Process Eng.*, 2024, **67**, 106209, DOI: 10.1016/j.jwpe.2024.106209.

53 Y. Jin, X. Mi, J. Qian, N. Ma and W. Dai, Modular Construction of an MIL-101(Fe)@MIL-100(Fe) Dual-Compartment Nanoreactor and Its Boosted Photocatalytic Activity toward Tetracycline, *ACS Appl. Mater. Interfaces*, 2022, **14**(42), 48285–48295, DOI: 10.1021/acsami.2c14489.

54 P. Zhang, X. Zhang, X. Zhao, *et al.*, Activation of peracetic acid with zero-valent iron for tetracycline abatement: the role of Fe(II) complexation with tetracycline, *J. Hazard. Mater.*, 2022, **424**(pt D), 127653, DOI: 10.1016/j.jhazmat.2021.127653.

55 D. Hao, Y. Chen, Y. Zhang, *et al.*, Nanocomposites of zero-valent iron@biochar derived from agricultural wastes for adsorptive removal of tetracyclines, *Chemosphere*, 2021, **284**, 131342, DOI: 10.1016/j.chemosphere.2021.131342.

56 Y. Song, C. Su, N. You, *et al.*, Nanocomposites of zero-valent Iron@Activated carbon derived from corn stalk for adsorptive removal of tetracycline antibiotics, *Chemosphere*, 2020, **255**, 126917, DOI: 10.1016/j.chemosphere.2020.126917.

57 A. M. Abdelfatah, M. Fawzy, M. E. El-Khouly, *et al.*, Efficient adsorptive removal of tetracycline from aqueous solution using phytosynthesized nano-zero valent iron, *J. Saudi Chem. Soc.*, 2021, **25**(12), 101365, DOI: 10.1016/j.jscs.2021.101365.

58 Q. Li, S. Zhao and Y. Wang, Mechanism of Oxytetracycline Removal by Coconut Shell Biochar Loaded with Nano-Zero-Valent Iron, *Int. J. Environ. Res. Publ. Health*, 2021, **18**(24), 13107, DOI: 10.3390/ijerph182413107.

59 G. Huang, M. Wang, Q. Liu, *et al.*, Efficient removal of tetracycline in water using modified eggplant straw biochar supported green nanoscale zerovalent iron: synthesis, removal performance, and mechanism, *RSC Adv.*, 2024, **14**, 3567–3577, DOI: 10.1039/d3ra08417e.

60 M. Yang, X. Chen, D. Ai, *et al.*, Sulfur-doped zero-valent iron supported on biochar for tetracycline adsorption and removal, *J. Clean. Prod.*, 2022, DOI: 10.1016/j.jclepro.2022.13476.

61 M. Fayazi and M. Ghanei-Motlagh, Enhanced performance of adsorptive removal of dibenzothiophene from model fuel over copper(II)-alginate beads containing polyethyleneterephthalate derived activated carbon, *J. Colloid Interface Sci.*, 2021, **604**, 517–525, DOI: 10.1016/j.jcis.2021.07.035.

62 L. Duan, H. Jiang, W. Wu, *et al.*, Defective iron based metal-organic frameworks derived from zero-valent iron for highly efficient fenton-like catalysis, *J. Hazard. Mater.*, 2023, **445**, 130426, DOI: 10.1016/j.jhazmat.2022.130426.

63 X. Li and J. Shi, Simultaneous adsorption of tetracycline, ammonium and phosphate from wastewater by iron and nitrogen modified biochar: kinetics, isotherm, thermodynamic and mechanism, *Chemosphere*, 2022, **293**, 133574, DOI: 10.1016/j.chemosphere.2022.133574.

64 M. Fayazi and E. Rezvannejad, Bio-inspired preparation of silver nanoparticles on nanostructured sepiolite clay: characterization and application as an effective adsorbent for methylene blue removal, *Inorg. Chem. Commun.*, 2023, **159**(9), 111786, DOI: 10.1016/j.inoche.2023.111786.

65 J. Wang, X. Wang, Y. Ji, *et al.*, Green electrospun Fe-based MOFs incorporated polyvinyl alcohol/carboxymethyl chitosan nanofibrous membranes for enhanced adsorption of tetracycline hydrochloride, *Int. J. Biol. Macromol.*, 2024, **279**, 135113, DOI: 10.1016/j.ijbiomac.2024.135113.

66 A. Liu, J. Liu, S. He, *et al.*, Bimetallic MOFs loaded cellulose as an environment friendly bioadsorbent for highly efficient tetracycline removal, *Int. J. Biol. Macromol.*, 2023, **225**, 40–50, DOI: 10.1016/j.ijbiomac.2022.11.321.

67 J. Cao, Z. Xiong and B. Lai, Effect of initial pH on the tetracycline (TC) removal by zero-valent iron: adsorption, oxidation and reduction, *Chem. Eng. J.*, 2018, **343**, 492–499, DOI: 10.1016/j.cej.2018.03.036.

68 S. Ghaedi, H. Rajabi, M. Hadi Mosleh and M. Sedighi, MOF biochar composites for environmental protection and pollution control, *Bioresour. Technol.*, 2025, **418**, 131982, DOI: 10.1016/j.biortech.2024.131982.